



Afterpulse correction for micro-pulse lidar to improve middle and upper tropospheric aerosol measurements

**HAILING XIE,^{1,2,*} ZHIEN WANG,^{1,2} TIAN ZHOU,³ KANG YANG,^{1,2}
XIAOHONG LIU,⁴ QIANG FU,⁵ DAMAO ZHANG,⁶ AND MIN DENG²**

¹*Department of Atmospheric and Oceanic Sciences, University of Colorado, Boulder, CO 80309, USA*

²*Laboratory for Atmospheric and Space Physics, University of Colorado, Boulder, CO 80303, USA*

³*Key Laboratory for Semi-Arid Climate Change of the Ministry of Education, College of Atmospheric Sciences, Lanzhou University, Lanzhou, Gansu 730000, China*

⁴*Department of Atmospheric Sciences, Texas A&M University, College Station, TX 77843, USA*

⁵*Department of Atmospheric Sciences, University of Washington, Seattle, WA 98195, USA*

⁶*Atmospheric Sciences and Global Change Division, Pacific Northwest National Laboratory, Richland, WA 99354, USA*

*hailing.xie@colorado.edu

Abstract: Micro-pulse lidar (MPL) measurements have been widely used in atmospheric research over the past few decades. However, the MPL afterpulse noise has a large impact on the MPL aerosol measurement in the middle and upper troposphere, and an effective correction method is still lacking. Here, a new afterpulse correction approach is presented by using measurements with low-level optically thick clouds to act as the lids blocking atmospheric signals beyond the clouds completely. Examples are provided to illustrate the effectiveness of this correction method. Using one-year 2014 MPL measurements at the U.S. Department of Energy Atmospheric Radiation Measurement (ARM) North Slope of Alaska (NSA) site, the impact of the correction on the aerosol measurements is quantified. The relative error (RE, %) of attenuated backscattering ratio (ABR) without the afterpulse correction is 30% and 190% at the height of 1.00 km and 9.00 km (AGL), and the RE is larger for weaker aerosol signals ($ABR < 2$). The RE of linear depolarization ratio (LDR), which is significantly higher than that of ABR for a given aerosol layer, is highly non-linear above 3.00 km, with a value of 300%-900% for weak aerosols ($ABR < 2$) above 3.00 km. Therefore, the afterpulse correction is critical for the middle and upper tropospheric aerosol observations. We demonstrated that our afterpulse correction can provide reasonable particle depolarization ratio (PDR) to properly identify dust aerosols. The newly developed method can be applied to long-term MPL measurements to support aerosol and mixed-phase/ice cloud interaction study at the NSA site.

© 2021 Optical Society of America under the terms of the [OSA Open Access Publishing Agreement](#)

1. Introduction

Atmospheric aerosols affect the Earth's energy budget by direct interaction with solar radiation through scattering and absorption [1,2]. Also, aerosols alter cloud microphysical characteristics indirectly by acting as cloud condensation nuclei (CCN) or ice-nucleating particles (INPs) – the so-called aerosol-cloud interactions (ACI) [3]. However, the change of planetary albedo stemming from ACI is still one of the largest uncertainties in the current climate predictions [4,5].

Dominant ACI mechanisms depend on cloud types [6]. Due to complex microphysical processes, the indirect effects of aerosols associated with mixed-phase clouds [7,8], connective clouds [9], and ice clouds [10,11] in the middle and upper troposphere remain poorly constrained. For example, the perturbations in INP concentrations dominate over changes in CCN concentrations in Arctic mixed-phase clouds [12]. In addition, the vertical distributions of aerosol load and types are crucial for ACI, especially in the vicinity of clouds [13–16]. Therefore, it is important

to accurately characterize middle and upper tropospheric aerosol properties to better understand their effects on the mixed-phase and ice clouds.

Lidar is a powerful tool for aerosol and cloud profiling in the troposphere [17–19], including ground-based, satellite-based and airborne observation platforms. Polarization techniques greatly expand the lidar capabilities for aerosol type determination, especially for dust detection [20]. For the last two decades, micro-pulse lidar (MPL) [21,22] has been widely used in routine aerosol and cloud measurements. Many ground-based MPL networks were built in various regions around the world, including the MPLNET [23], U.S. Department of Energy (DOE) Atmospheric Radiation Measurement (ARM) Program sites [24] and Chinese sites [25–28]. It has been widely used for atmospheric studies, such as the planetary boundary layer height retrieval [29], aerosol distribution analysis [30], cloud detection and typing [31,32], precipitation detection [33], the optical properties of different aerosol mixtures with depolarization [34]. These studies have demonstrated that MPL performs well for atmospheric applications.

However, due to the imperfection of the semiconductor for the Avalanche Photo-Diode (APD) detectors used by MPLs, a small fraction of electron-hole pairs become trapped during an avalanche event [35,36]. If the APD is biased above breakdown before the traps have fully emptied, the detrapping electron-hole pairs can initiate another avalanche [37–39]. This effect, known as the afterpulse noise, introduces distortion in MPL detected signals. The afterpulse noise can typically causes unneglectable errors in signal and depolarization measurements, especially in middle and upper troposphere [37]. Afterpulsing behavior of APDs has been poorly investigated, because of the complex dependency of detector characterizations on operational conditions [39]. For example, the APD stability is very sensitive to the applied external voltage and to operation temperature. Moreover, each semiconductor device is unique and it possesses unique properties caused by degree of purity of a crystal and other technological factors [39,40]. To improve the MPL data quality and understand ACI better, it is critical to correct the afterpulse effects for the ground-based MPL measurements.

A new method of afterpulse correction is proposed for the polarized MPL in this study. Section 2 provides a general introduction of routine corrections for MPL data processing and current status of MPL afterpulse corrections. Section 3 elaborates the methodology in this study, and section 4 further discusses the application and evaluation of the method. Finally, section 5 presents the summary and conclusions.

2. MPL afterpulse noise

2.1. Effects and properties of the afterpulse noise in MPL

For the polarized MPL, required signal corrections in different polarization states can be written as:

$$P_{corrected_i}(r) = P_{raw_i}(r) * D(P_{raw_i}) - B_{raw_i} - A_{raw_i}(r, E) \quad (1)$$

where $P_{raw}(r)$ is the signal return in photoelectron counts per second at range r , $P_{corrected}(r)$ is the corrected signal, $D(P_{raw})$ is the detector deadtime correction factor, $A_{raw}(r, E)$ is the detector afterpulse correction, E represents the emit energy of the laser pulse, and B_{raw} is the solar background signal. The superscript “i” denotes different polarized states.

For the polarized MPL, linear depolarization ratio (LDR) can be calculated as [41]:

$$\delta^v(r) = \frac{P_{corrected_cr}(r)}{P_{corrected_co}(r) + P_{corrected_cr}(r)} \quad (2)$$

where ‘cr’ and ‘co’ indicate crosspol and copol polarized states, respectively.

In Eq. (1), the afterpulse noise correction is a major height-dependent term among the three noise sources. Thus, neglecting afterpulse effect induces the wrong slopes of lidar signal and biased LDRs with height [42]. In general, the molecular measurements under the clear-sky

condition can be used to evaluate the effectiveness and robustness of the afterpulse correction. An example of MPL clear-sky measurements is presented in Fig. 1. The measured signals (green solid line in Fig. 1(a)) and LDR (green solid line in Fig. 1(b)) profiles without afterpulse corrections (ACs) indicate that there is no aerosol layer structures. But measured signals (green solid line in Fig. 1(a)) decrease slower with altitude than the expected molecular signals (blue dashed line in Fig. 1(a)) and the difference of slopes is more significant with the increasing altitude. It suggests that there is ‘an extra signal’ in the lidar returns, and the effect of the ‘extra signal’ is obvious in the middle and upper troposphere. This is a typical sign of the effect of the afterpulse noise [21,43]. Physically, the expected molecular LDR is constant with height [44]. In Fig. 1(b), the measured LDR (green solid line) without ACs is increasingly linear with increasing height (Fig. 1(b)), which is not consistent with expected molecular LDRs.

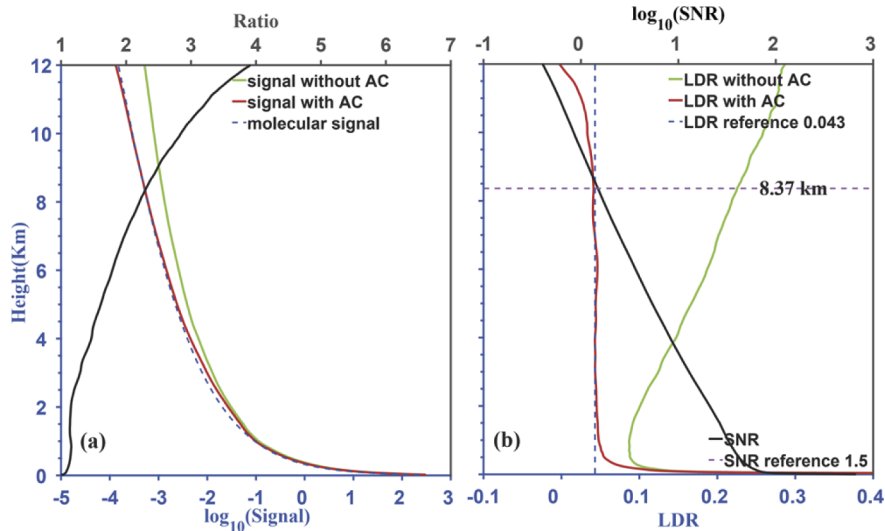


Fig. 1. (a) The measured signal profiles without/with afterpulse correction (ACs) (green/red solid lines) and expected molecular signal profile (blue dashed line), ratio of signal profiles without and with ACs (black solid line), (b) The measured LDR profiles without/with ACs (green/red solid lines) and LDR reference profile (blue dashed line), SNR profile (black solid line) and SNR reference profile (purple dashed line) from MPL during 06:00-10:00 UTC on November 07, 2014 at NSA site. The afterpulse corrections are realized using the new method proposed in this study. The signal profiles have been smoothed by performing a 100 range gate (15m) moving average.

An accurate correction should make the lidar measurement profiles and the expected molecular profiles consistent in molecular signal slopes [45] and constant molecular LDR with height [44]. The signals with the ACs method discussed below can achieve these goals as presented in Fig. 1.

Notably, afterpulsing is a direct function of the energy associated with each transmitted pulse as noted in [21]. Therefore, energy normalization should be performed for calculated afterpulse noise to reduce the effect of unavoidable perturbations in transmitted pulse energies (due to laser aging, dust, etc.). This is shown as:

$$A_{raw_E}(r) = A_{raw}(r) \times \frac{E}{E_m} \quad (3)$$

where $A_{raw_E}(r)$ is the final energy-normalized afterpulse correction, E is the shot energy monitor value (mJ) during the MPL measurement, and E_m is the average energy monitor value during the

chosen MPL measurements period for determining the ACs. MPL system records transmitted laser energy together with atmospheric returns.

2.2. Previous afterpulse correction methods

Isolating afterpulse signal is best accomplished when the system is operated in a ‘blocked’ configuration, where atmospheric backscatter and ambient background counts are eliminated. In such a scenario, signal measured beyond the blocking point (in terms of time) is the afterpulse noise. This can be achieved in a laboratory setting (i.e., a dark room when the system is pointed at a target) [22,46], or more easily by applying a lid to the transceiver to eliminate the background light [21,39,47]. It is noticeable that the experimental method needs to be processed in near-real time. Obviously, it is not applicable in the historical measurement data.

Besides that, Welton et al. [43] introduced a method based on historical observation data. They chose the data period under the clean condition and the lidar returns were assumed to represent the pure Rayleigh scattering. In this condition, the actual measured lidar signal $P_L(r)$ and Rayleigh lidar signal $P_R(r)$ have the linear relationship:

$$P_L(r) = C \cdot O(r)P_R(r) + A(r) \quad (4)$$

C is the assumed lidar system constant. By fitting as a function of with Eq. (4), the y intercept was used to construct the afterpulse function $A(r)$ and the slope was used to determine the overlap function $O(r)$. However, the method is unstable because of the need of determining multiple parameters at the same time.

Other relevant works simply provide the concept or the similar methods as mentioned previously [48,49]. Thus, practical afterpulse correction methods for historical MPL data processing are still lacking.

3. Methodology

3.1. ARM MPL observations

This study is motivated by the needs to characterize the aerosol distributions at DOE ARM sites with long-term MPL measurements. The MPL is an eye-safe and highly sensitive lidar system of measuring all-day vertical backscattering profiles from optically thin clouds and aerosols and molecules. Polarized MPL systems have been operating regularly since August 2006. More extensive descriptions of MPL system are given by Campbell et al. [21], Welton et al. [47], and Flynn et al. [41]. In this study, MPL (532 nm) measurements at ARM North Slope of Alaska (NSA) site, located just to the northeast of Utqiagvik (formerly Barrow), Alaska (71.3°N, 156.6°W, 8 m), which had MPL measurements since 1998, are used. The one-year period data from January 2014 to December 2014 was selected to evaluate the effectiveness of the new correction method. In addition, the pressure, temperature, and relative humidity from radiosondes are also used to calculate lidar molecular backscattering signals.

To identify aerosol layers using MPL measurements, the atmospheric feature boundary needed to be identified when signal-to-noise (SNR) [50] was more than 1.5. Then, a fixed threshold (e.g., attenuated backscattering ratio (ABR) > 6) was used to screen cloud layers, and the profiles with $ABR \leq 6$ was regarded as aerosol profiles.

The ABR, LDR, and particle depolarization ratio (PDR) quantities of aerosol were used for analysis. The ABR is calculated as:

$$ASR(r) = (\beta_p(r) + \beta_m(r)) \exp[-2 \int_0^z \alpha_p(r') dr'] \exp[-2 \int_0^z \alpha_m(r') dr'] / \beta_m(r) \quad (5)$$

where $\beta_p(r)$ and $\beta_m(r)$ are the particulate and molecule backscatter coefficient, respectively. $\alpha_p(r)$ and $\alpha_m(r)$ are the particulate and molecular extinction coefficient.

PDR is calculated as [20]:

$$\delta^P = \frac{(1 + \delta^m)\delta^v R - (1 + \delta^v)\delta^m}{(1 + \delta^m)R - (1 + \delta^v)} \quad (6)$$

where δ^m is molecular LDR, which is constant with height [44,51,52]. It is set to be 0.05 in this study. The lidar backscattering ratio R is approximated by ABR, which could introduce some uncertainties in PDR estimations when aerosol optical depths are high. But for this study, this is not a significant issue because the afterpulse noise has weaker impacts under high aerosol loading conditions.

In the meantime, relative error (RE) of ABR and LDR used to evaluate the new afterpulse correction method is defined as:

$$RE_j = \frac{j_{without_AC} - j_{with_AC}}{j_{with_AC}} \quad (7)$$

where 'j' denotes the ABR or LDR variables, 'AC' denotes afterpulse noise.

3.2. Afterpulse correction method

To quantify the afterpulse noise, MPL measurements with low-level optically thick clouds were chosen in this study. The low-level optically thick clouds act as the lids that can block atmospheric signals beyond the clouds completely. Under this condition, MPL signals above the complete signal attenuation level do not contain any return from the atmosphere and measured signals are due to the afterpulse noise. The difference between using low-level optically thick clouds and lids to measure the afterpulse noise is the time when they block atmospheric signals. Lids can be used to block MPL atmospheric returns completely prior to the first range bin, while low-level optically thick clouds have specific base height and thickness. Therefore, there is a gap in height-dependent afterpulse noise using optically thick clouds as the lid compared using a physical lid. Although the laser pulses are attenuated quickly by the low-level optically thick clouds, measurements within 500m or more above the apparent cloud top height (which can be located approximately with absolute negative slope of signal less than 8 (count/ μ s/km) [45]) have to be excluded to avoid possible multiple scattering effects. The lowest height level with useable signal for afterpulse noise analysis is determined by finding a height level with less than 4 continuous bins (15 m vertical resolution) with absolute signal slopes less than 1.1 (count/ μ s/km) starting at the 'the apparent cloud top height' upward. If the height difference between these two heights is less than 500 m, we move the lowest height level at 500 m above the apparent cloud top height. For a case illustrated in Fig. 2, the gap is about 1.00 km.

In Fig. 2, the red and black solid lines show the mean MPL copol and crosspol profiles during 06:00-07:00 UTC on September 15, 2014 at NSA site. Due to the presence of low-level optically thick clouds, the apparent cloud top height is about 0.50 km, while the actual cloud top height is nearly 7.00 km based on cloud radar measurements (not presented here). MPL measured signals above 1.00 km are used to the afterpulse noise. To fill the afterpulse noise gap below 1.00 km, the data between 1.00-3.00 km (a 2 km range above the lowest useful data level) was used to fit as $\log_{10}(P) = aH^2 + bH + c$, where P is the range-uncorrected signal, H is the height, a, b and c are coefficients to be determined, then the fit function is extended to the height below 1.00 km. The selection of fitting function was guided by the afterpulse signal determined in [21]. A 2 km height range provide enough data points to fitting reliably for extrapolation. The fit profile and observed signal profile above 1.00 km were merged at an altitude with the minimum difference between the two profiles to form a complete afterpulse noise profile. Finally, a mean laser pulse energy needs to be recorded to use the derived afterpulse noise profile as indicated in Eq. (3).

Considering that the afterpulse noise could change with the MPL hardware and environment, low-level optically thick clouds with liquid water path (LWP) $>20\text{g/m}^2$ could be used to get the

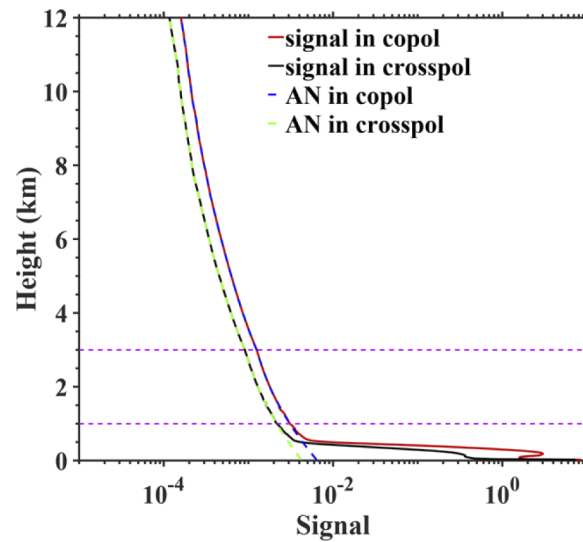


Fig. 2. MPL original signal (count/ μ s, red and black solid lines) and determined afterpulse noise (AN) (count/ μ s, blue and green dashed lines) profiles during 06:00-07:00 UTC on September 15, 2014 at the NSA site.

afterpulse noise profiles under different periods to support the analysis of long-term historical MPL observations. Assuming cloud droplet effective radius of $10\ \mu\text{m}$, the cloud layer optical depth is 3 with LWP of 20g/m^2 . Two-way lidar attenuation through this cloud (e^{-6}) is $\sim 0.25\%$. Thus, molecular returns above cloud top are significantly attenuated and weaker than the afterpulse signals.

4. Evaluation and applications

An example of using the proposed afterpulse correction is given in Fig. 1. As illustrated in Fig. 1(a), the slope of corrected signals (red solid line) is consistent with the slope of molecular signal (blue dashed line) within 0.00-12.00 km except for 1.00-4.00 km where there are weak aerosols. As we know, the troposphere extends from the surface of the Earth to a height of approximately 30,000 ft (~ 9.14 km) at the Polar Regions [53]. The ratio of signals without and with the ACs (black solid line) increases with height from ~ 1.00 at the surface to ~ 4.00 at 12.00 km, which indicates that the contribution of afterpulse is significant in the middle and upper troposphere [21,43]. Without the ACs, LDR nearly increases linearly with height from ~ 0.08 to ~ 0.28 (green solid line, in Fig. 1(b)), which is non-physical. The correction makes LDR (red solid line) values fall into a reasonable range when SNR (black solid line) is above 1.5 (below 8.37 km). LDR is almost consistent ~ 0.043 at heights of 1.00-8.37 km, which is consistent with the theory that the molecular LDR is constant with height [44,52,54].

To further illustrate the effectiveness of the approach, comparisons of ABR and LDR with and without the afterpulse correction for a whole day with multiple aerosol layers are shown in Fig. 3. With ABR measurements, multi-layer aerosol structure, the upper tropospheric aerosol layers (~ 7.00 km) (due to the lower solar background during the nighttime), the middle tropospheric aerosol layer (~ 4.50 km), the low tropospheric aerosol layer (~ 1.50 km) and the aerosols in the boundary layer (~ 0.50 km), can be identified before (Fig. 3(a)) and after (Fig. 3(b)) the corrections. However, there are significant differences in the aerosol loads as indicated by ABR values with and without the afterpulse corrections. It is clear that afterpulse noise leads to overestimations of aerosols from MPL measurements in the middle and upper troposphere. While the aerosols in

the boundary layer can be detected from the LDR measurements, it is hard to distinguish the structures of middle and upper tropospheric aerosol layers based on LDRs without the afterpulse correction (Fig. 3(c)). It suggests that the difference between both LDRs (Figs. 3(c) and 3(d)) may depend on the height and aerosol types. Compared with ABR changes, Figs. 3(c) and 3(d) show that the corrections result in even larger LDR value corrections, which is critical for aerosol type identifications. With the afterpulse corrections, LDR and ABR measurements show consistent aerosol layer structures in the whole troposphere.

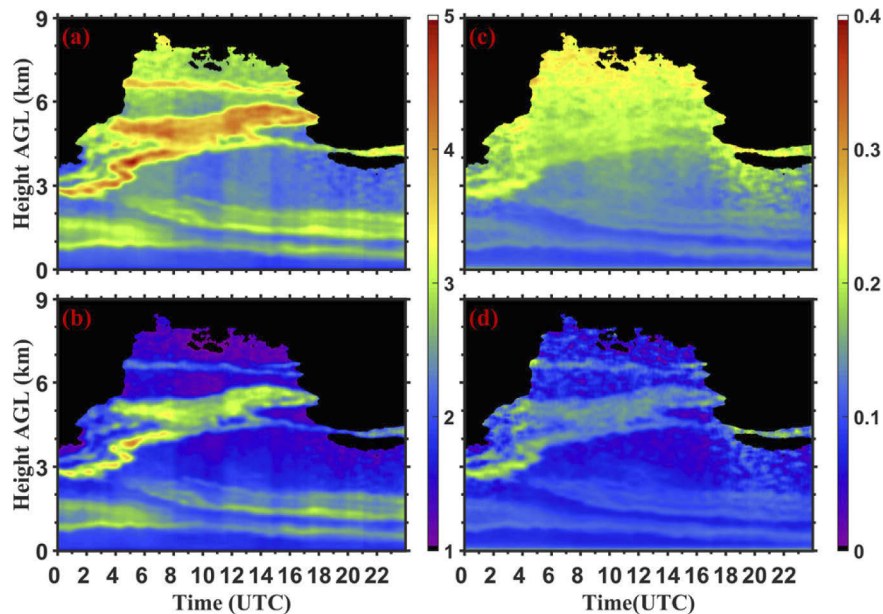


Fig. 3. ABR (a) without afterpulse correction and (b) with afterpulse correction, and LDR (c) without afterpulse correction and (d) with afterpulse correction on March 24, 2014 for MPL at NSA site

To prove the stability of the new afterpulse correction method, the method was applied to MPL measurements during 2014 at the NSA site with 6 periods of suitable low-level clouds selected for afterpulse noise determinations (see Table 1). The determined afterpulse noise profiles are used to be temporally close to MPL measurements corrections. There are a total of 1296 hourly aerosol profiles. Comparing ABR and LDR without (Figs. 4(a) and 4(c)) and with (Figs. 4(b) and 4(d)) the corrections, improvements of data quality are obvious and it is consistent with the results shown in Figs. 1 and 3. In addition, ABRs without the afterpulse correction are difficult to identify the middle and upper tropospheric aerosol layer structures, especially from February to April. This could lead to incorrect identifications of the clear-sky boundaries to correctly set boundary values using the Fernald solution [55] to retrieve aerosol vertical distributions with elastic lidar measurements, and further results in a wrong estimation of aerosol radiative impacts [56]. Meanwhile, there is an obvious increase in LDR with altitude without the afterpulse correction above 2.00 km. It also shows that LDR corrections (difference between Figs. 4(c) and 4(d)) are larger than ABR corrections (difference between Figs. 4(a) and 4(b)), which implies that the afterpulse noise produces the larger errors in LDR than in ABR.

After the corrections, aerosol annual cycles in the middle and upper troposphere at the NSA site can be explored accurately. For example, high frequent occurrences of dust aerosols in spring and winter, especially in spring (Fig. 4(d) and 4(b)), can be clearly identified as a part of the known Arctic haze [57]. The seasonal variation derived from MPL measurements after

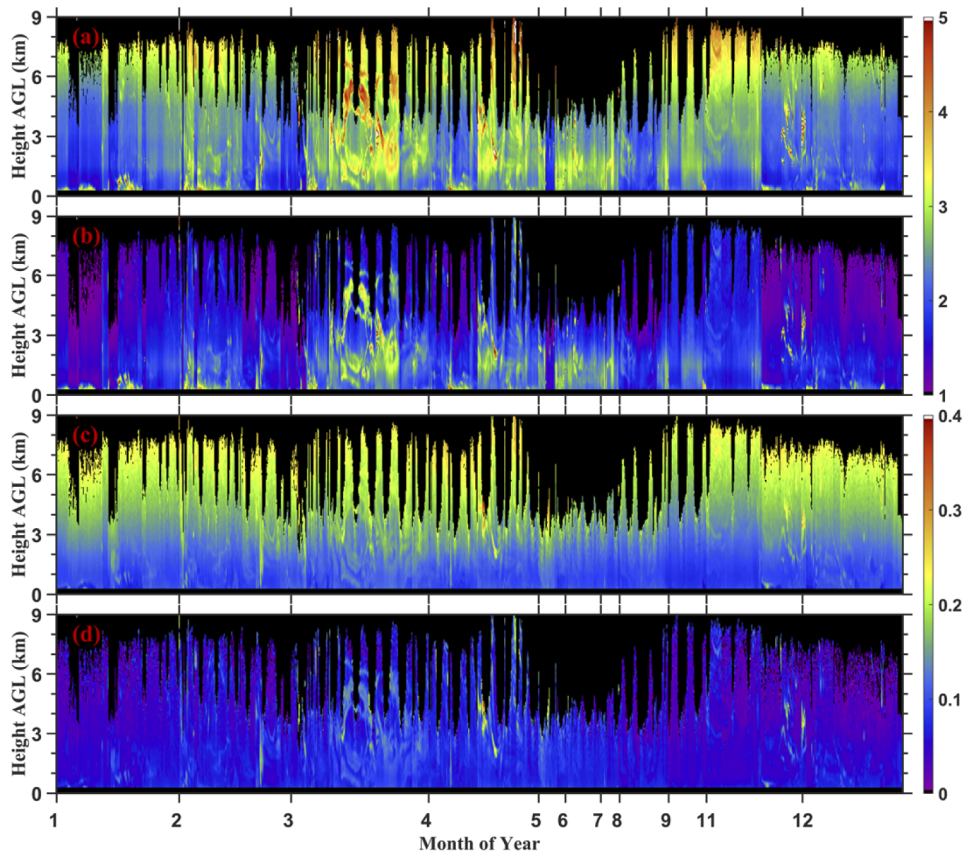


Fig. 4. ABR aerosol available profiles (temporal resolution: 1h) (a) without afterpulse correction and (b) with afterpulse correction, LDR aerosol available profile (c) without afterpulse correction and (d) with afterpulse correction for MPL from January to December of 2014 at NSA site. The number of aerosol available profiles in different months are different.

Table 1. MPL observation cases selected for the afterpulse noise determinations during 2014 at the NSA site

cases	1	2	3	4	5	6
Date	01/04	02/04	04/27	09/15	10/23	12/06
time (UTC)	15:00-16:00	6:00-9:00	8:30-9:30	6:00-7:00	11:00-12:00	15:00-16:00

afterpulse correction is consistent with other relevant results [58]. But a detailed study of arctic aerosol annual cycle is beyond the scope of this paper.

To show the effect of afterpulse noise on ABR and LDR quantitatively, Fig. 5 shows the REs (%) of ABR (5a) and LDR (5b) as a function of height and ABRs based on the results in Fig. 4. As indicated in Fig. 5, the REs for aerosol below 1.00 km are generally within 30%, thus it is possible to study boundary layer aerosols with MPL measurements without the afterpulse corrections, especially when ABRs are above 2. However, with height increase, REs increase dramatically.

ABR value increases from ~30% at 1.00 km to ~190% at 9.00 km. It suggests that the effect of afterpulse on ABR increases with height, which is consistent with the results of Campbell et al. [21]. The influence of the afterpulse noise on ABR estimations decreases with increasing aerosol

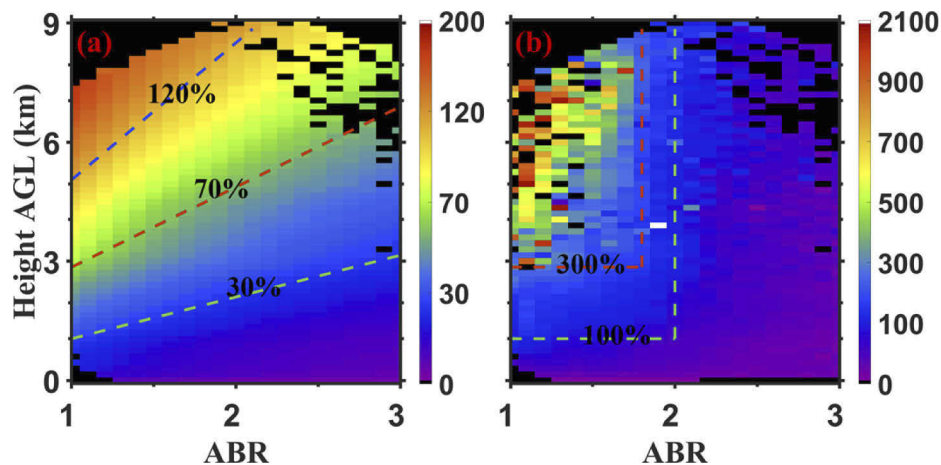


Fig. 5. The relative errors (REs: %) in (a) ABR and (b) LDR due to the afterpulse noise based on aerosol profiles in Fig. 4. The x-axis is ABR after the correction. The green, red and blue dashed lines indicate the variation trend of RE=30%, RE=70% and RE=120% in (a); while green and red dashed line indicate RE=100% and RE=300% in (b)

load. For example, if the RE=30% is considered to be acceptable, MPL data are acceptable below 1.00 km for the weaker aerosols ($ABR \approx 1$) and below 3.00 km for the stronger aerosols ($ABR \geq 3$). By comparing the slope of three RE lines (30%-dashed green line, 70%-dashed red line and 120%-dashed blue line), the slope gets larger with height. It implies that the afterpulse effects on ABRs increase with height more slowly than with increasing ABR.

At the higher altitudes (>1.00 km) and the lower aerosol loads ($ABR < 2$), REs of LDR vary dramatically from $\sim 100\%$ to 900% . The REs of LDR increase from 100% (dashed green line) in the boundary layer to 300% (dashed red line) in the middle troposphere. Above 3.00 km, the REs of LDR increase with height non-linearly, with larger errors for the measurements at the higher altitude with the weaker aerosols. REs of LDR (Fig. 5(b)) are significantly larger than REs of ABR (Fig. 5(a)) at the same height and ABR value. Therefore, it is necessary to perform the afterpulse corrections to MPL polarization measurements to accurately detect and quantify non-spherical aerosol particles.

The corresponding distributions of feature properties (scattering properties: backscattering coefficient and linear depolarization ratio, which can be estimated by ABR and PDR coarsely) are used to discriminate the cloud and aerosol [59,60]. Figure 6(a) and 6(b) illustrates the improvements of the afterpulse correction on PDR estimations based on the corrected data in Fig. 4. The distribution of PDRs with afterpulse corrections as a function of afterpulse corrected ABRs is consistent with results shown in Thorsen and Fu [59]. Moreover, PDR is an indispensable quantity for the discrimination of dust particle from other aerosol types [61,62]. Before the correction, PDRs calculated are biased high ($PDR \sim 0.5-2.5$), especially for the weaker aerosols ($ABR < 2$). The correction can bring PDR into the normal ranges (0-0.15) for aerosols, which is consistent with results in [61-63].

To evaluate the PDR and ABR relationship observed after the corrections, collocated CALIPSO measurements based on the CALIPSO Level 2 5km aerosol profile products [64] were compared with MPL results in Fig. 6(c) and 6(d). The CALIPSO ABR and PDR within $5.0^\circ \times 5.0^\circ$ centered at the NSA site are averaged to compare with MPL measurements. MPL data are averaged from 3-hourly observations over the grid box with 60 m vertical resolution. Due to high cloud occurrence around the NSA site, only 28 collocating cases were found. The results in Fig. 6(d) above shows that collocated MPL (circle symbols) and CALIPSO (square symbols)

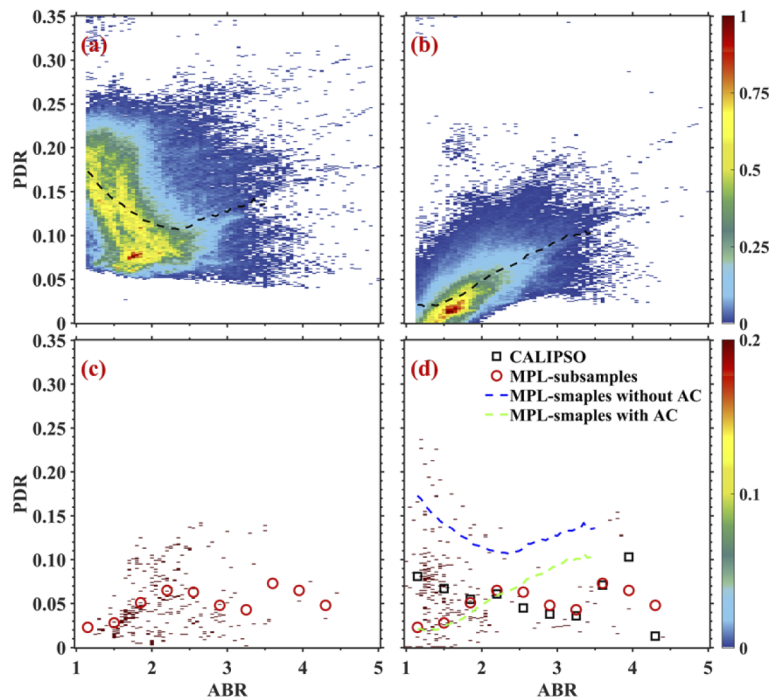


Fig. 6. The histograms of aerosol ABR with afterpulse corrections and PDR (a) without afterpulse corrections and (b) with afterpulse corrections based on MPL measurements in Fig. 4. The histograms of aerosol ABR with afterpulse corrections and PDR with afterpulse corrections based on collocating measurements of MPL (c) and CALIPSO (d) during 2014. Frequency is normalized by the highest occurrence. The lines are the mean PDR values for each specific ABR bin width.

measurements follows the same trends closely other than under small ABR ($ABR < 1.8$) values, and the MPL PDR without afterpulse correction (blue line) is biased much higher for the same ABR values. This result confirms that the proposed afterpulse correction brings the aerosol PDR into a correct range. Several uncertainties could attribute to the noticeable difference for the weak aerosol ($ABR < 1.8$). First, MPL is possibly slightly overestimated, which could lead to underestimating PDR. Secondly, for weak aerosol layers, noisy CALIPSO signals would lead to overestimated aerosol PDR. Considering these potential uncertainties, MPL and CALIPSO measurements under small ABR values agree reasonably well.

5. Summary and conclusions

A new afterpulse correction method is proposed for polarized MPL measurements. The new approach uses MPL measurements in the presence of optically thick low-level clouds to derive the afterpulse noise at the altitude that is 500m above the apparent cloud top and a fitting approach to estimate the afterpulse noise below. The new method is simple and robust enough to be applied to long-term historical MPL measurements. Examples show that the method can correct the obvious MPL measurement bias and provide signals with consistent slope with the expected molecular signals (Fig. 1(a)) and constant LDRs with height under clear-sky conditions and improved ABR and LDR estimations for aerosol layers.

To demonstrate the feasibility of the new approach for long-term MPL data analysis, the approach was applied to MPL measurements at the NSA site in 2014. Six MPL measurement

periods were selected to provide temporally dependent MPL afterpulse noise profile estimations. The six afterpulse noise profiles are very close with the ratios of standard deviations and means below 0.1 for both channels. Thus, it is enough to have seasonal afterpulse noise profiles under normally MPL operations, such as DOE/ARM. It is important to have a new afterpulse noise profile determined after any MPL hardware changes.

The corrected ABRs and LDRs show a more reliable aerosol annual cycle at the NSA site. The REs of ABRs and LDRs increase with height and could overestimate up to 190% and 900% at 9.00 km, respectively. Although REs of ABR and LDR decrease with increasing ABR, the afterpulse effects are still significant when $ABR < 3$ and above 3.00 km. The correction also can bring aerosol PDR values with a reasonable range to make non-spherical aerosol particles identification possible with MPL polarization measurements. The comparison of collocated MPL and CALIPSO lidar measurements confirms that the improved aerosol PDRs are in a correct range. These results confirm that the afterpulse correction is essential for middle and upper tropospheric aerosol characterizations with MPL measurements.

For the afterpulse corrections, the signal quality is critical. For example, noisy signals could lead to negative LDR estimations, which should be rejected for further analysis. For nighttime MPL, hourly-averaged MPL measurements offer stable aerosol characterizations up to 8.00 km in 2014. The afterpulse effects will decrease with MPL signal magnitudes. The results here are based on the MPL system deployed at the NSA site in 2014. For the newer MPL systems with improved signal-to-noise ratio at the upper troposphere, the afterpulse effect could be much smaller.

The approach can be applied to different generation MPL systems, which are widely deployed worldwide to improve middle and upper tropospheric aerosols. After the afterpulse corrections and the overlap function corrections, the Fernald approach can be applied to determine aerosol backscattering and extinction coefficients. Our ongoing effort is to process nearly 20-year MPL measurements at the NSA site to understand the changing arctic environments. Combining MPL retrieving aerosol properties with multi-sensors deriving ice and mixed-phase cloud can be used to study aerosol-cloud interactions.

Funding. U.S. Department of Energy (DE-SC0020510).

Acknowledgments. We acknowledge support by the U.S. Department of Energy (DOE) Atmospheric System Research (ASR) Program (grants DE-SC0020510). Ground-based remote sensing data are obtained from the Atmospheric Radiation Measurement Program (ARM) sponsored by the DOE (<http://www.archive.arm.gov/>). Many thanks are also extended to the anonymous reviewers for their comments.

Disclosures. The authors declare no conflicts of interest.

Data availability. Data underlying the results presented in this paper are not publicly available at this time but may be obtained from the authors upon reasonable request.

References

1. U. Lohmann and J. Feichter, "Global indirect aerosol effects: a review," *Atmos. Chem. Phys.* **5**(3), 715–737 (2005).
2. W. K. Tao, J. P. Chen, Z. Q. Li, C. Wang, and C. D. Zhang, "Impact of Aerosols on Convective Clouds and Precipitation," *Rev. Geophys.* **50**, 1–62 (2012).
3. J. H. Seinfeld, C. Bretherton, K. S. Carslaw, H. Coe, P. J. DeMott, E. J. Dunlea, G. Feingold, S. Ghan, A. B. Guenther, R. Kahn, I. Kraucunas, S. M. Kreidenweis, M. J. Molina, A. Nenes, J. E. Penner, K. A. Prather, V. Ramanathan, V. Ramaswamy, P. J. Rasch, A. R. Ravishankara, D. Rosenfeld, G. Stephens, and R. Wood, "Improving our fundamental understanding of the role of aerosol-cloud interactions in the climate system," *Proc Natl Acad Sci USA* **113**(21), 5781–5790 (2016).
4. N. Bellouin, J. Quaas, E. Gryspeerdt, S. Kinne, P. Stier, D. Watson-Parris, O. Boucher, K. S. Carslaw, M. Christensen, A. L. Daniau, J. L. Dufresne, G. Feingold, S. Fiedler, P. Forster, A. Gettelman, J. M. Haywood, U. Lohmann, F. Malavelle, T. Mauritsen, D. T. McCoy, G. Myhre, J. Mulmenstadt, D. Neubauer, A. Possner, M. Rugenstein, Y. Sato, M. Schulz, S. E. Schwartz, O. Sourdeval, T. Storelvmo, V. Toll, D. Winker, and B. Stevens, "Bounding Global Aerosol Radiative Forcing of Climate Change," *Reviews of Geophysics* **58**(1), e2019RG000660 (2020).
5. I. L. McCoy, D. T. McCoy, R. Wood, L. Regayre, D. Watson-Parris, D. P. Grosvenor, J. P. Mulcahy, Y. Hu, F. A. Bender, P. R. Field, K. S. Carslaw, and H. Gordon, "The hemispheric contrast in cloud microphysical properties constrains aerosol forcing," *Proc Natl Acad Sci USA* **117**(32), 18998–19006 (2020).

6. J. W. Fan, Y. Wang, D. Rosenfeld, and X. H. Liu, "Review of Aerosol-Cloud Interactions: Mechanisms, Significance, and Challenges," *J. Atmos. Sci.* **73**(11), 4221–4252 (2016).
7. M. S. Norgren, G. de Boer, and M. D. Shupe, "Observed aerosol suppression of cloud ice in low-level Arctic mixed-phase clouds," *Atmos. Chem. Phys.* **18**(18), 13345–13361 (2018).
8. Y. Shi and X. H. Liu, "Dust Radiative Effects on Climate by Glaciating Mixed-Phase Clouds," *Geophys. Res. Lett.* **46**(11), 6128–6137 (2019).
9. B. Zhao, Y. Wang, Y. Gu, K. N. Liou, J. H. Jiang, J. W. Fan, X. H. Liu, L. Huang, and Y. L. Yung, "Ice nucleation by aerosols from anthropogenic pollution," *Nat. Geosci.* **12**(8), 602–607 (2019).
10. R. Patnaude and M. H. Diao, "Aerosol Indirect Effects on Cirrus Clouds Based on Global Aircraft Observations," *Geophys. Res. Lett.* **47**(10), e2019GL086550 (2020).
11. B. Zhao, K. N. Liou, Y. Gu, J. H. Jiang, Q. B. Li, R. Fu, L. Huang, X. H. Liu, X. J. Shi, H. Su, and C. L. He, "Impact of aerosols on ice crystal size," *Atmos. Chem. Phys.* **18**(2), 1065–1078 (2018).
12. A. Solomon, G. de Boer, J. M. Creamean, A. McComiskey, M. D. Shupe, M. Maahn, and C. Cox, "The relative impact of cloud condensation nuclei and ice nucleating particle concentrations on phase partitioning in Arctic mixed-phase stratocumulus clouds," *Atmos. Chem. Phys.* **18**(23), 17047–17059 (2018).
13. Z. Lu, X. H. Liu, Z. B. Zhang, C. Zhao, K. Meyer, C. Rajapakse, C. L. Wu, Z. F. Yang, and J. E. Penner, "Biomass smoke from southern Africa can significantly enhance the brightness of stratocumulus over the southeastern Atlantic Ocean," *Proc Natl Acad Sci USA* **115**(12), 2924–2929 (2018).
14. Y. Wang, X. J. Zheng, X. Q. Dong, B. K. Xi, P. Wu, T. Logan, and Y. L. Yung, "Impacts of long-range transport of aerosols on marine-boundary-layer clouds in the eastern North Atlantic," *Atmos. Chem. Phys.* **20**(23), 14741–14755 (2020).
15. M. S. Diamond, A. Dobracki, S. Freitag, J. D. S. Griswold, A. Heikkila, S. G. Howell, M. E. Kacarab, J. R. Podolske, P. E. Saide, and R. Wood, "Time-dependent entrainment of smoke presents an observational challenge for assessing aerosol-cloud interactions over the southeast Atlantic Ocean," *Atmos. Chem. Phys.* **18**(19), 14623–14636 (2018).
16. H. Yu, M. Chin, H. Bian, T. Yuan, J. M. Prospero, A. H. Omar, L. A. Remer, D. M. Winker, Y. Yang, Y. Zhang, and Z. Zhang, "Quantification of trans-Atlantic dust transport from seven-year (2007–2013) record of CALIPSO lidar measurements," *Remote Sensing of Environment* **159**, 232–249 (2015).
17. H. Baars, A. Ansmann, K. Ohneiser, M. Haarig, R. Engelmann, D. Althausen, I. Hanssen, M. Gausa, A. Pietruczuk, A. Szkop, I. S. Stachlewska, D. X. Wang, J. Reichardt, A. Skupin, I. Mattis, T. Trickl, H. Vogelmann, F. Navas-Guzman, A. Haeffele, K. Acheson, A. A. Ruth, B. Tatarov, D. Müller, Q. Y. Hu, T. Podvin, P. Goloub, I. Veselovskii, C. Pietras, M. Haefelin, P. Freville, M. Sicard, A. Comeron, A. J. F. Garcia, F. M. Menendez, C. Cordoba-Jabonero, J. L. Guerrero-Rascado, L. Alados-Arboledas, D. Bortoli, M. J. Costa, D. Dionisi, G. L. Liberti, X. Wang, A. Sannino, N. Papagiannopoulos, A. Boselli, L. Mona, G. D'Amico, S. Romano, M. R. Perrone, L. Belegante, D. Nicolae, I. Grigorov, A. Gialitaki, V. Amiridis, O. Soupiona, A. Papayannis, R. E. Mamouri, A. Nisantzi, B. Heese, J. Hofer, Y. Y. Schechner, U. Wandinger, and G. Pappalardo, "The unprecedented 2017–2018 stratospheric smoke event: decay phase and aerosol properties observed with the EARLINET," *Atmos. Chem. Phys.* **19**(23), 15183–15198 (2019).
18. Z. Wang and M. Menenti, "Challenges and Opportunities in Lidar Remote Sensing," *Front. Remote Sens.* **2**, 3 (2021).
19. T. Zhou, H. Xie, T. Jiang, J. Huang, J. Bi, Z. Huang, and J. Shi, "Seasonal characteristics of aerosol vertical structure and autumn enhancement of non-spherical particle over the semi-arid region of northwest China," *Atmos. Environ.* **244**, 117912 (2020).
20. V. Freudenthaler, M. Esselborn, M. Wiegner, B. Heese, M. Tesche, A. Ansmann, D. Mueller, D. Althausen, M. Wirth, A. Fix, G. Ehret, P. Knippertz, C. Toledano, J. Gasteiger, M. Garhammer, and A. Seefeldner, "Depolarization ratio profiling at several wavelengths in pure Saharan dust during SAMUM 2006," *Tellus B: Chemical and Physical Meteorology* **61**(1), 165–179 (2009).
21. J. R. Campbell, D. L. Hlavka, E. J. Welton, C. J. Flynn, D. D. Turner, J. D. Spinhirne, V. S. Scott, and I. H. Hwang, "Full-time, eye-safe cloud and aerosol lidar observation at atmospheric radiation measurement program sites: Instruments and data processing," *J. Atmos. Oceanic Technol.* **19**(4), 431–442 (2002).
22. E. J. Welton and J. R. Campbell, "Micropulse lidar signals: Uncertainty analysis," *J. Atmos. Oceanic Technol.* **19**(12), 2089–2094 (2002).
23. E. J. Welton, J. R. Campbell, J. D. Spinhirne, and V. S. Scott, "Global monitoring of clouds and aerosols using a network of micro-pulse lidar systems," *P Soc Photo-Opt Ins* **4153**, 151–158 (2001).
24. D. N. Kafle and R. L. Coulter, "Micropulse lidar-derived aerosol optical depth climatology at ARM sites worldwide," *J. Geophys. Res. Atmos.* **118**(13), 7293–7308 (2013).
25. K. Qin, L. X. Wu, M. S. Wong, H. Letu, M. Y. Hu, H. M. Lang, S. J. Sheng, J. Y. Teng, X. Xiao, and L. M. Yuan, "Trans-boundary aerosol transport during a winter haze episode in China revealed by ground-based Lidar and CALIPSO satellite," *Atmos. Environ.* **141**, 20–29 (2016).
26. J. Shen and N. Cao, "Comprehensive observation and analysis of aerosol optical properties and vertical distribution in Nanjing, China," *Atmos. Environ.* **239**, 117767 (2020).
27. H. Xie, T. Zhou, Q. Fu, J. Huang, Z. Huang, J. Bi, J. Shi, B. Zhang, and J. Ge, "Automated detection of cloud and aerosol features with SACOL micro-pulse lidar in northwest China," *Opt. Express* **25**(24), 30732–30753 (2017).
28. T. Zhou, H. Xie, J. Bi, Z. Huang, J. Huang, J. Shi, B. Zhang, and W. Zhang, "Lidar Measurements of Dust Aerosols during Three Field Campaigns in 2010, 2011 and 2012 over Northwestern China," *Atmosphere* **9**(5), 173 (2018).

29. J. R. Lewis, E. J. Welton, A. M. Molod, and E. Joseph, "Improved boundary layer depth retrievals from MPLNET," *J. Geophys. Res. Atmos.* **118**(17), 9870–9879 (2013).
30. S. P. Parajuli, G. L. Stenchikov, A. Ukhov, I. Shevchenko, O. Dubovik, and A. Lopatin, "Aerosol vertical distribution and interactions with land/sea breezes over the eastern coast of the Red Sea from lidar data and high-resolution WRF-Chem simulations," *Atmos. Chem. Phys.* **20**(24), 16089–16116 (2020).
31. J. R. Lewis, J. R. Campbell, S. A. Stewart, I. Tan, E. J. Welton, and S. Lolli, "Determining cloud thermodynamic phase from the polarized Micro Pulse Lidar," *Atmos. Meas. Tech.* **13**(12), 6901–6913 (2020).
32. J. R. Lewis, J. R. Campbell, E. J. Welton, S. A. Stewart, and P. C. Haftings, "Overview of MPLNET, Version 3, Cloud Detection," *J. Atmos. Ocean. Tech.* **33**(10), 2113–2134 (2016).
33. S. Lolli, G. Vivone, J. R. Lewis, M. Sicard, E. J. Welton, J. R. Campbell, A. Comerón, L. P. D'Adderio, A. Tokay, A. Giunta, and G. Pappalardo, "Overview of the New Version 3 NASA Micro-Pulse Lidar Network (MPLNET) Automatic Precipitation Detection Algorithm," *Remote Sens.* **12**(1), 71 (2020).
34. C. Cordoba-Jabonero, M. Sicard, A. Ansmann, A. del Aguila, and H. Baars, "Separation of the optical and mass features of particle components in different aerosol mixtures by using POLIPHON retrievals in synergy with continuous polarized Micro-Pulse Lidar (P-MPL) measurements," *Atmos. Meas. Tech.* **11**(8), 4775–4795 (2018).
35. B. J. Pichler and S. I. Ziegler, "CHAPTER 14 - Photodetectors," in *Emission Tomography*, M. N. Wernick and J. N. Aarsvold, eds. (Academic Press, San Diego, 2004), pp. 255–267.
36. D. Renker, "Geiger-mode avalanche photodiodes, history, properties and problems," *Nucl Instrum Meth A* **567**(1), 48–56 (2006).
37. P. W. Cottle, "Aerosol type analysis with single wavelength, dual polarization elastic LIDAR," Ph.D. dissertation (University of British Columbia, 2016).
38. K. Jensen, P. Hopman, E. Duerr, E. Dauler, J. Donnelly, S. Groves, L. Mahoney, K. McIntosh, K. Molvar, and A. Napoleone, "Predicting afterpulsing in free-running, Geiger-mode avalanche photodiodes at 1.06 μm wavelength," in *Conference on Lasers and Electro-Optics*, (Optical Society of America, 2006), CThD6.
39. I. Razenkov, "Characterization of a Geiger-mode avalanche photodiode detector for high spectral resolution lidar," M.S. Thesis (University of Wisconsin–Madison, 2010).
40. A. W. Ziarkash, S. K. Joshi, M. Stipcevic, and R. Ursin, "Comparative study of afterpulsing behavior and models in single photon counting avalanche photo diode detectors," *Sci. Rep.* **8**(1), 5076 (2018).
41. C. J. Flynn, A. Mendoza, Y. H. Zheng, and S. Mathur, "Novel polarization-sensitive micropulse lidar measurement technique," *Opt. Express* **15**(6), 2785–2790 (2007).
42. D. Flynn, C. Sivaraman, J. Comstock, and D. Zhang, "Micropulse Lidar Cloud Mask (MPLCMASK) Value-Added Product for the Fast-Switching Polarized Micropulse Lidar Technical Report," No. DOE/SC-ARM/TR-098. (DOE Office of Science Atmospheric Radiation Measurement (ARM) user facility, 2020).
43. E. J. Welton, K. J. Voss, H. R. Gordon, H. Maring, A. Smirnov, B. Holben, B. Schmid, J. M. Livingston, P. B. Russell, and P. A. Durkee, "Ground-based lidar measurements of aerosols during ACE-2: Instrument description, results, and comparisons with other ground-based and airborne measurements," *Tellus B* **52**(2), 636–651 (2000).
44. A. Behrendt and T. Nakamura, "Calculation of the calibration constant of polarization lidar and its dependency on atmospheric temperature," *Opt. Express* **10**(16), 805–817 (2002).
45. Z. Wang and K. Sassen, "Cloud type and macrophysical property retrieval using multiple remote sensors," *J. Appl. Meteorol.* **40**(10), 1665–1682 (2001).
46. K. J. Voss, E. J. Welton, P. K. Quinn, J. Johnson, A. M. Thompson, and H. R. Gordon, "Lidar measurements during Aerosols99," *J. Geophys. Res.: Atmos.* **106**(D18), 20821–20831 (2001).
47. E. J. Welton, K. J. Voss, P. K. Quinn, P. J. Flatau, K. Markowicz, J. R. Campbell, J. D. Spinhirne, H. R. Gordon, and J. E. Johnson, "Measurements of aerosol vertical profiles and optical properties during INDOEX 1999 using micropulse lidars," *J. Geophys. Res.-Atmos.* **107** (D19) 8019 (2002).
48. R. Tiruchirapalli, "Micropulse lidar observations of free tropospheric aerosols over the atmospheric radiation measurement site at Barrow, Alaska," M.S. Thesis (MS, University of Alaska Fairbanks, 2006).
49. J. R. Campbell, D. L. Hlavka, J. D. Spinhirne, V. Stanley Scott, and D. D. Turner, "Operational processing and cloud boundary detection from Micro Pulse Lidar data," in *NASA CONFERENCE PUBLICATION*, (NASA, 1998), 119–122.
50. V. A. Kovalev and W. E. Eichinger, *Elastic lidar: theory, practice, and analysis methods* (John Wiley & Sons, 2004).
51. M. I. Mishchenko, J. M. Dlugach, and L. Liu, "Linear depolarization of lidar returns by aged smoke particles," *Appl. Opt.* **55**(35), 9968–9973 (2016).
52. A. Nisantzi, R. E. Mamouri, A. Ansmann, and D. Hadjimitsis, "Injection of mineral dust into the free troposphere during fire events observed with polarization lidar at Limassol, Cyprus," *Atmos. Chem. Phys.* **14**(22), 12155–12165 (2014).
53. J. G. Speight, "1 - Water systems," in *Natural Water Remediation*, (Butterworth-Heinemann, 2020), pp. 1–51.
54. H. Baars, P. Seifert, R. Engelmann, and U. Wandinger, "Target categorization of aerosol and clouds by continuous multiwavelength-polarization lidar measurements," *Atmos. Meas. Tech.* **10**(9), 3175–3201 (2017).
55. F. G. Fernald, "Analysis of Atmospheric Lidar Observations - Some Comments," *Appl. Opt.* **23**(5), 652–653 (1984).
56. A. K. Mishra, I. Koren, and Y. Rudich, "Effect of aerosol vertical distribution on aerosol-radiation interaction: A theoretical prospect," *Heliyon* **1**(2), e00036 (2015).

57. P. K. Quinn, G. Shaw, E. Andrews, E. G. Dutton, T. Ruoho-Airola, and S. L. Gong, "Arctic haze: current trends and knowledge gaps," *Tellus B: Chemical and Physical Meteorology* **59**(1), 99–114 (2007).
58. R. Engelmann, A. Ansmann, K. Ohneiser, H. Griesche, M. Radenz, J. Hofer, D. Althausen, S. Dahlke, M. Maturilli, I. Veselovskii, C. Jimenez, R. Wiesen, H. Baars, J. Bühl, H. Gebauer, M. Haarig, P. Seifert, U. Wandinger, and A. Macke, "Wildfire smoke, Arctic haze, and aerosol effects on mixed-phase and cirrus clouds over the North Pole region during MOSAiC: an introduction," *Atmos. Chem. Phys.* **21**(17), 13397–13423 (2021).
59. T. J. Thorsen and Q. Fu, "Automated Retrieval of Cloud and Aerosol Properties from the ARM Raman Lidar. Part II: Extinction," *J. Atmos. Ocean. Tech.* **32**(11), 1999–2023 (2015).
60. T. Luo, Z. E. Wang, D. M. Zhang, X. H. Liu, Y. Wang, and R. M. Yuan, "Global dust distribution from improved thin dust layer detection using A-train satellite lidar observations," *Geophys. Res. Lett.* **42**(2), 620–628 (2015).
61. S. Groß, V. Freudenthaler, M. Wirth, and B. Weinzierl, "Towards an aerosol classification scheme for future EarthCARE lidar observations and implications for research needs," *Atmos. Sci. Lett.* **16**(1), 77–82 (2015).
62. T. Shibata, K. Shiraiishi, M. Shiobara, S. Iwasaki, and T. Takano, "Seasonal Variations in High Arctic Free Tropospheric Aerosols Over Ny-Alesund, Svalbard, Observed by Ground-Based Lidar," *J. Geophys. Res. Atmos.* **123**(21), 12353–12367 (2018).
63. H. Baars, T. Kanitz, R. Engelmann, D. Althausen, B. Heese, M. Komppula, J. Preissler, M. Tesche, A. Ansmann, U. Wandinger, J. H. Lim, J. Y. Ahn, I. S. Stachlewska, V. Amiridis, E. Marinou, P. Seifert, J. Hofer, A. Skupin, F. Schneider, S. Bohlmann, A. Foth, S. Bley, A. Pfuller, E. Giannakaki, H. Lihavainen, Y. Viisanen, R. K. Hooda, S. N. Pereira, D. Bortoli, F. Wagner, I. Mattis, L. Janicka, K. M. Markowicz, P. Achtert, P. Artaxo, T. Pauliquevis, R. A. F. Souza, V. P. Sharma, P. G. van Zyl, J. P. Beukes, J. Y. Sun, E. G. Rohwer, R. R. Deng, R. E. Mamouri, and F. Zamorano, "An overview of the first decade of Polly(NET): an emerging network of automated Raman-polarization lidars for continuous aerosol profiling," *Atmos. Chem. Phys.* **16**(8), 5111–5137 (2016).
64. S. A. Young and M. A. Vaughan, "The Retrieval of Profiles of Particulate Extinction from Cloud-Aerosol Lidar Infrared Pathfinder Satellite Observations (CALIPSO) Data: Algorithm Description," *J. Atmos. Ocean. Tech.* **26**(6), 1105–1119 (2009).